



# The Effect of CWTSAW on the Toughness of Heavy-Gauge X70 – Part II: Correlating Microstructure with Charpy Toughness

The effect of martensite-austenite morphology on Charpy toughness for cold-wire tandem submerged-arc welded X70 steel was studied

BY T. REN, J. B. WISKEL, G. LEHNHOFF, D. G. IVEY, L. LI, L. COLLINS, M. GAUDET, E. WILLETT, AND H. HENEIN

## Abstract

The effect of martensite-austenite (MA) constituent morphology, prior austenite grain size, fracture length, and notch placement on the Charpy toughness and micro-hardness in the heat-affected zone (HAZ) of heavy-gauge (19.1 mm thick) X70 microalloyed steel welded by cold-wire tandem submerged-arc welding (CWTSAW) was studied. In Part I, a series of single-pass CWTSAW samples were made using cold wire feed rates (effective heat input) of 0 mm/s (2.9 kJ/mm), 16.9 mm/s (2.6 kJ/mm), and 33.9 mm/s (2.3 kJ/mm). In Part II, the absorbed energy values at  $-10^{\circ}\text{C}$  and  $-30^{\circ}\text{C}$  ranged widely from 240 J (max) to 8 J (min) for effective heat inputs of 2.9 kJ/mm and 2.3 kJ/mm. The higher Charpy energies for the 2.9 kJ/mm and 2.3 kJ/mm samples tended to occur when the notch center was located in the fine-grained HAZ (FGHAZ), and much of the crack propagated through the FGHAZ. The lower Charpy energies for the same heat inputs occurred when the notch center was positioned in the coarse-grained HAZ (CGHAZ), which had a significant amount of coarse-stringer MA constituents. The 2.6 kJ/mm samples had consistently high absorbed energy results ( $> 190$  J), whether the notch center was positioned in the coarse-grained HAZ or the FGHAZ. The number of coarse-stringer MA constituents in the CGHAZ of 2.6 kJ/mm sample was the lowest. A severity parameter (SP) was developed to correlate the severity of coarse-stringer MA and crack length in the CGHAZ/FGHAZ. The SP value increased as the number of coarse-stringer MA and fracture length in

the CGHAZ increased, which correlated to reduced Charpy toughness.

## Keywords

- Cold Wire Tandem Submerged-Arc Welding
- Martensite-Austenite Morphology
- Prior Austenite Grains
- Charpy Toughness
- Micro-Hardness

## Introduction

Cold-wire tandem submerged-arc welding (CWTSAW) is a welding process consisting of three electrodes: a lead electrode, a trail electrode, and a cold electrode (no current is applied to this wire). CWTSAW was developed for heavy gauge microalloyed steel line pipe ( $> 17$  mm) to reduce the effective heat input of tandem submerged-arc welding (TSAW) and to maintain and improve the coarse-grained heat-affected zone (CGHAZ) toughness.

In Part I of this two-part article (Ref. 1), the effects of effective heat input (cold wire feed rate) on the area (Area) and aspect ratio (AR) distribution of the martensite-austenite (MA) constituents in the CGHAZ and fine-grained heat-affected zone (FGHAZ) and the size of the prior austenite grains (PAGs) in the CGHAZ were studied. The PAG size and MA constituent morphology (Area and AR distribution) were measured using optical microscopy. The average PAG size was reduced from  $139\ \mu\text{m}$  to  $83\ \mu\text{m}$  as the effective heat input was decreased from 2.9 kJ/mm (0 mm/s cold wire feed rate) to 2.3 kJ/mm (33.9 mm/s cold wire feed rate). The total number of MA constituents and the Area fraction of MA in the CGHAZ was lowest for the intermediate heat input of 2.6 kJ/mm (16.9 mm/s cold wire feed rate). This behavior was

attributed to a balance between duration above  $A_{c1}$  and the cooling rate, which minimized the coarse MA constituents in the CGHAZ of 2.6 kJ/mm samples. This paper (Part II) continues with the previous work, correlating measured MA morphology distribution, PAG size distribution, and crack length with Charpy impact energies and hardness values.

Charpy impact energies measured from Gleeble-simulated CGHAZ regions for X70 pipeline steels depend on PAG size and MA morphology (Refs. 2, 3). Combining coarse PAG and concentrated MA regions resulted in low absorbed energy. The concentrated MA regions were a mixture of massive and elongated MA constituents that formed at the PAG boundary and are referred to as local brittle zones (Ref. 4). However, only a limited amount of quantitative correlations between MA morphology/PAG size and Charpy impact toughness profiles (energy values, crack path, and notch placement) in the CGHAZ of CWTSAW heavy gauge welds have been done.

The work presented in this paper (Part II) aims to establish the quantitative effect of MA morphology and PAG size, altered by cold wire feed rate, on the Charpy impact energy and crack path of heavy gauge (19.1 mm thick) X70 CWTSAW welds. A series of CWTSAW trials were carried out on heavy gauge (19.1 mm thick) X70 steel using three different cold wire feed rate levels: 0 mm/s, 16.9 mm/s, and 33.9 mm/s, which corresponded to effective heat inputs of 2.9 kJ/mm, 2.6 kJ/mm, and 2.3 kJ/mm, respectively. The effective heat input decreased as the cold wire feed rate increased due to more energy consumed by cold wire fusion. Detailed calculations of the effective heat input for each weld have been reported in a previous study (Ref. 5) by Ren, one of the authors of this paper. CGHAZ Charpy impact toughness (from 28°C and -60°C) and micro-hardness values of the heat-affected

zone (HAZ)/weld metal (WM) region were measured for each weld. The crack paths and notch placement for tested Charpy V-notched (CVN) samples were characterized using optical microscopy (OM), and fracture surfaces were examined using scanning electron microscopy (SEM). Charpy impact energies of the HAZ will be discussed based on the measured distance of the notch center to the fusion boundary ( $D_{NF}$ ) and crack path length in the HAZ. The results and discussion presented in this paper provide a quantitative correlation between MA and PAG size and HAZ Charpy toughness for heavy gauge X70 line pipe steel.

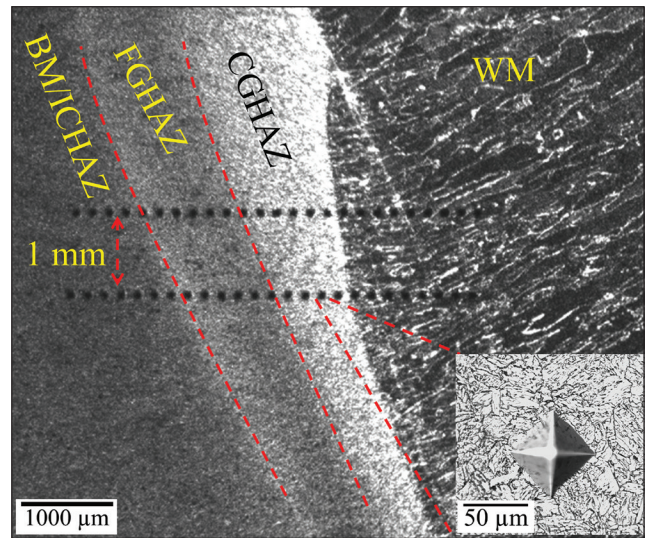


Fig. 1 – Micro-hardness traverse across the 2.9 kJ/mm joint.

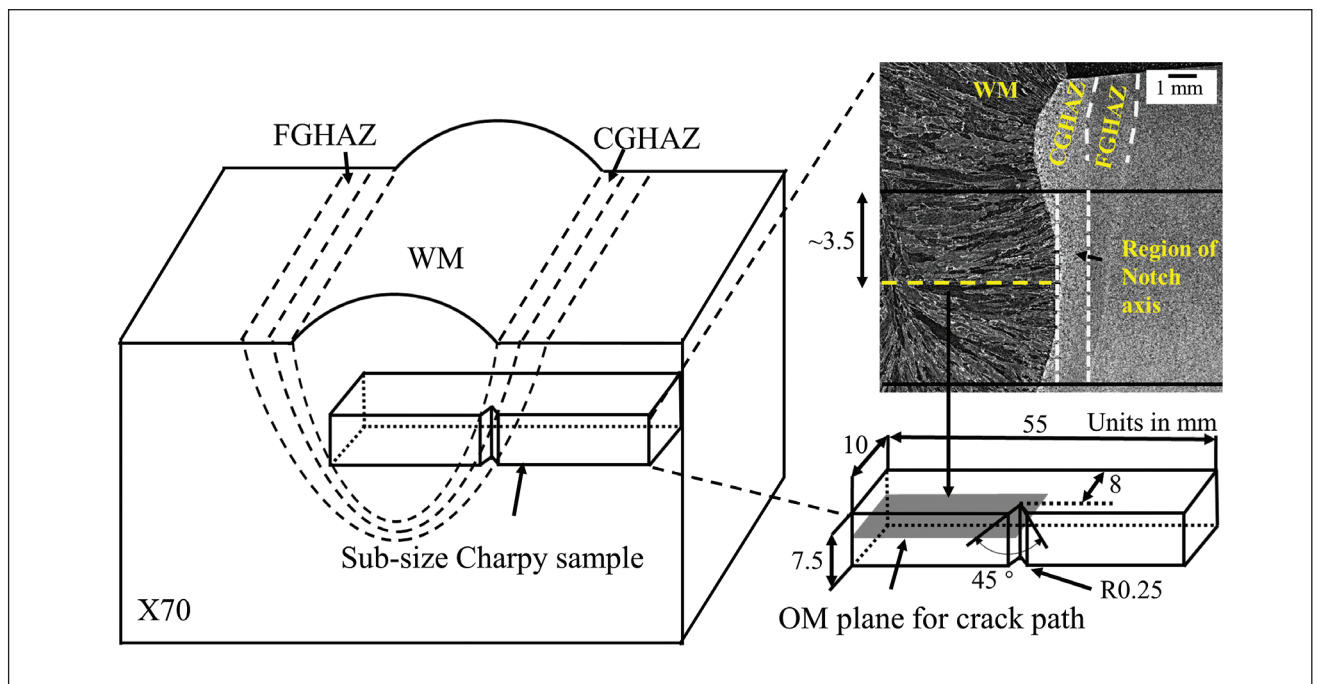


Fig. 2 – Schematic and the 2.6 kJ/mm joint image of sub-size Charpy V-notch (CVN) specimen and optical microscopy (OM) plane for crack path analysis.

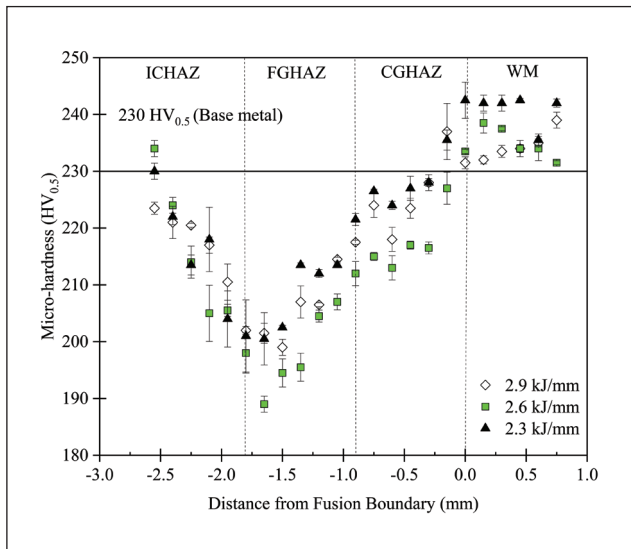


Fig. 3 – Micro-hardness values within the WM, CGHAZ, FGHAZ, ICHAZ, and the BM as a function of effective heat input.

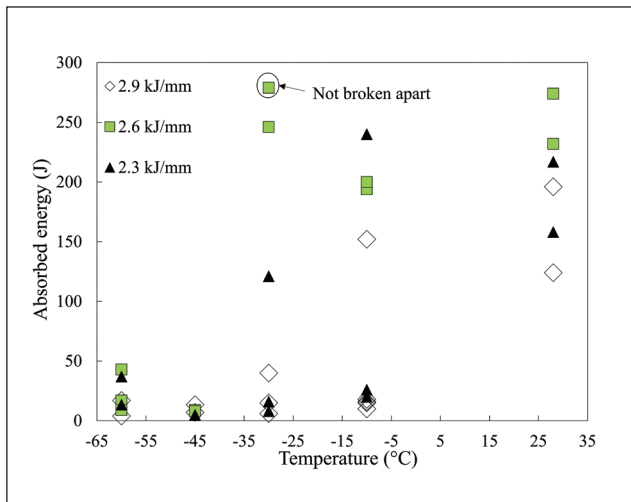


Fig. 4 – Charpy absorbed energy as a function of testing temperature and effective heat input.

## Experimental Procedure

The CWTSAW process consisted of lead, trail, and cold electrodes. Positive direct current electrodes and alternating current square wave modes were selected for the lead and trail electrodes. The current was not applied to the cold electrode. The composition of the X70 steel studied, the filler wire, the detailed CWTSAW configurations (bevel design, electrodes angular position, and stick-out length), and the microstructural characterization results were presented in Part I of this two-part article (Ref. 1). Micro-hardness and impact toughness testing will be described here.

## Micro-Hardness

Metallographic samples were polished and etched with 4% Nital to show the HAZ and WM boundaries. Vickers hardness measurements were taken in the base metal (BM), HAZ, and WM, as illustrated in Fig. 1 (Ref. 6). Two indentation lines (4 mm below the weld surface) contained a total of 50 indents from each weld sample with a minimum 10 to 12 indentations in each of the WMs and CGHAZs. A 0.5 kgf ( $HV_{0.5}$ ) and a dwell time of 10 s were used. The distance between two indentation lines (1 mm) and the size of an indent ( $\approx 50 \mu\text{m}$ ) are shown in Fig. 1.

## Impact Toughness

Sub-size CVN specimens (7.5 mm  $\times$  10 mm  $\times$  55 mm) with a 45 deg opening angle and 0.25 mm V-notch radius were machined along the transverse direction at the quarter thickness ( $\sim 4$  mm below the weld surface) of the weld according to ASTM E23-12C, *Standard Test Methods for Notched Bar Impact Testing of Metallic Materials* (Ref. 7). The Charpy tests were performed on the sub-size CVN specimens at 28°C,  $-10^\circ\text{C}$ ,  $-30^\circ\text{C}$ ,  $-45^\circ\text{C}$ , and  $-60^\circ\text{C}$ . The machined specimens were macro-etched with 5% Nital to show the HAZ and WM boundaries. The notch axis of CVN specimens was then located in the region from the fusion boundary to the interface of the CGHAZ and FGHAZ due to the 0.25 mm radius of the V-notch. Figure 2 shows the location of the extracted specimen, the notch axis region, and the sectioned plane at the middle thickness of the specimen for notch placement and crack path analysis by OM. In addition, the fracture surfaces of tested CVN specimens were examined by SEM.

## Results

### Micro-Hardness

The average micro-hardness values (six measurements) for the WM, CGHAZ, FGHAZ, inter-critical HAZ (ICHAZ), and BM, as a function of distance from the fusion line, are shown in Fig. 3. The micro-hardness of the BM was  $\approx 230 HV_{0.5}$ , which is indicated as a horizontal solid line in Fig. 3. The error bars for each measurement correspond to one standard deviation. The highest micro-hardness region for all welds was in the WM. The lowest micro-hardness region for all welds was at the FGHAZ/ICHAZ interface. The micro-hardness in the CGHAZ was consistently higher than the micro-hardness in the FGHAZ for all welds. This was attributed to the bainitic microstructure in the CGHAZ compared with polygonal ferrite in the FGHAZ. The 2.6 kJ/mm samples had consistently lower micro-hardness values in both the CGHAZ and FGHAZ compared with the 2.9 kJ/mm and 2.3 kJ/mm samples.

The micro-hardness values for the 2.9 kJ/mm and 2.3 kJ/mm samples ( $\approx 235 HV_{0.5}$ ) at a distance of  $-0.15$  mm from the fusion boundary were higher than the micro-hardness values for the 2.6 kJ/mm sample ( $\approx 228 HV_{0.5}$ ) at an equivalent distance. OM micrographs were taken from the same location. This micro-hardness difference was partially attributed to the difference in the area fraction of MA in the CGHAZ for

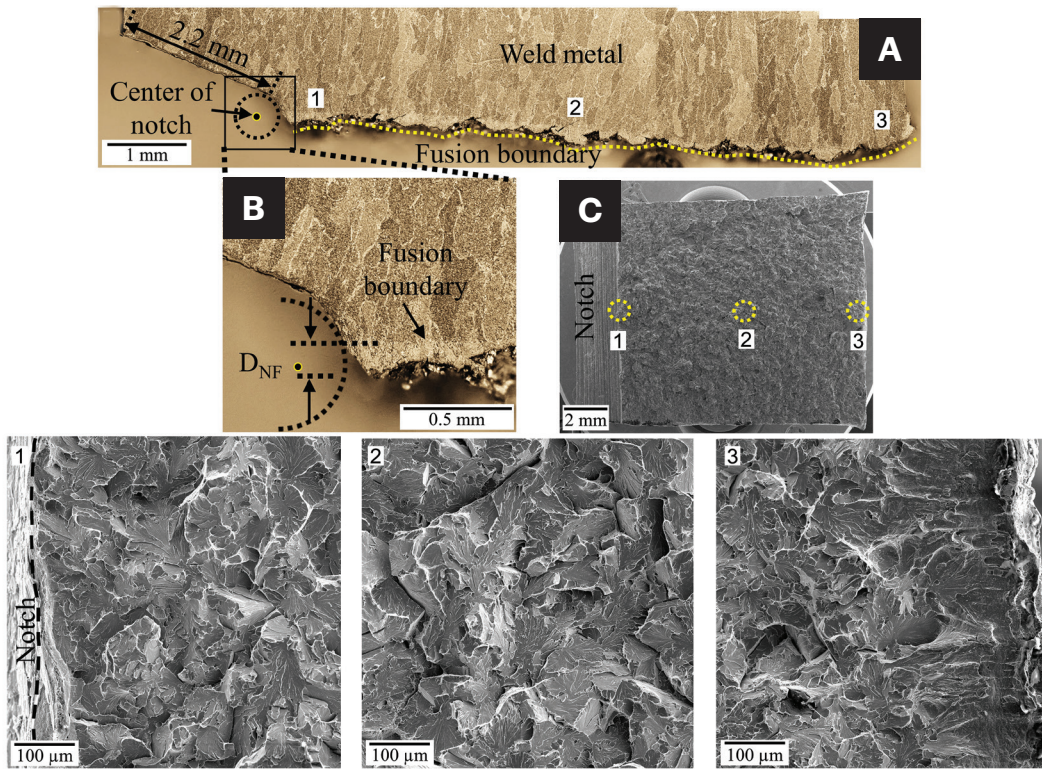


Fig. 5 – Charpy specimen for the 2.9 kJ/mm sample tested at  $-10^{\circ}\text{C}$  (16 J): A – Optical crack path profile at the middle thickness plane; B – magnified image of notch tip region; C – SEM SE images at the fracture surface locations labeled 1, 2, and 3.

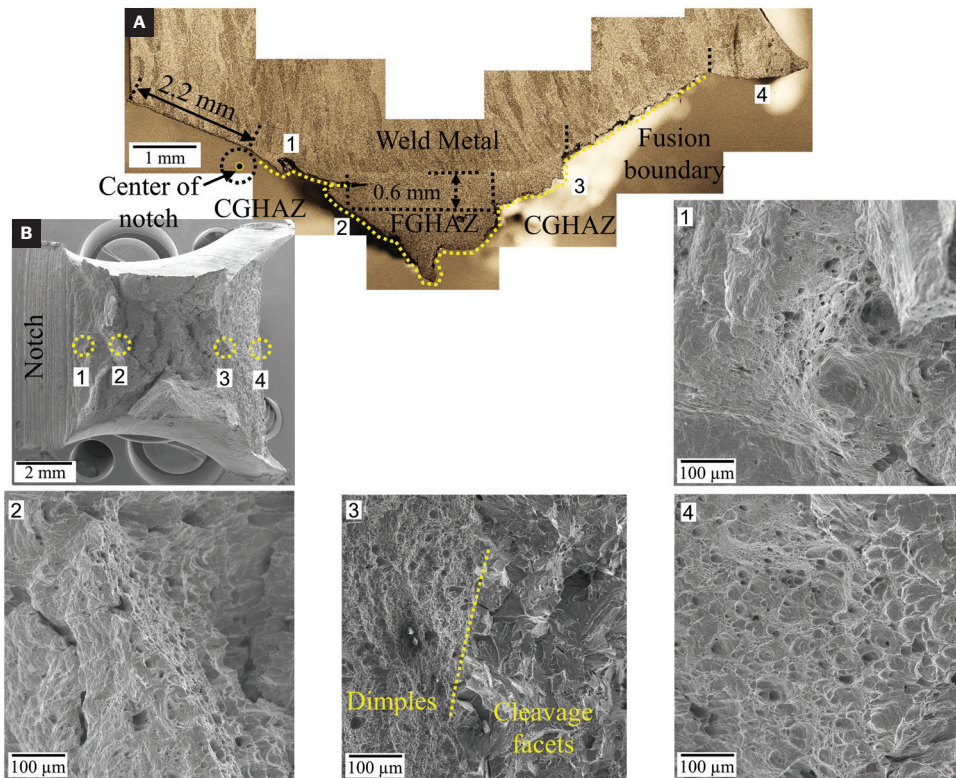


Fig. 6 – Charpy specimen for the 2.6 kJ/mm sample at  $-10^{\circ}\text{C}$  (194 J): A – Optical crack path profile at the middle thickness plane; B – SEM SE images at the fracture surface locations labeled 1, 2, 3, and 4.

**Table 1 – Measured Crack Length in the CGHAZ, FGHAZ, and BM of All CVN Samples at 28°C, –10°C, and –30°C**

Temperature (°C)	Samples	Absorbed Energy CE (J)	Measured Crack Length				Distance (notch/fusion) $D_{NF}$ (mm)
			$L_{F/CG\_C}$ (mm)	$L_{CG\_D}$ (mm)	$L_{FG}$ (mm)	$L_{Total}$ (mm)	
28	2.9 kJ/mm	124	4.6	–	3.7	8.3	0.75
	2.6 kJ/mm	232	3.6	5.4	–	9	0.22
	2.3 kJ/mm	158	4.4	–	6.7	11.1	0.61
–10	2.9 kJ/mm	16	8.05	–	–	8.05	0.1
		152	3.7	–	5.0	8.7	0.83
	2.6 kJ/mm	200	3.1	2.3	4.3	9.7	0.47
		194	3.5	5.5	3.0	12.0	0.2
	2.3 kJ/mm	20	8.1	–	–	8.1	0.16
		240	0.86	–	9.4	10.3	0.74
–30	2.9 kJ/mm	40	7.5	–	0.8	8.4	0.25
		6	8.18	–	–	8.18	0.04
		15	8.04	–	–	8.04	0.11
	2.6 kJ/mm	246	–	0.65	14.2*	14.9	0.69
		16	8	–	0.5	8.5	0
	2.3 kJ/mm	121	5.4	–	4.8	10.2	0.86
		8	8.05	–	–	8.05	0.1

\* $L_{FG}$  for the 2.6 kJ/mm sample at –30°C is the sum of the measured crack lengths in the FGHAZ and ICHAZ/BM region.

all welds, which was presented in the “MA Characterization” section of Part I (Ref. 1).

### Charpy Impact Toughness

The absorbed energy for the CVN samples as a function of test temperature is shown in Fig. 4. The 2.6 kJ/mm samples welded using a cold wire feed rate of 16.9 mm/s had a high absorbed energy (> 240 J) at a testing temperature of –30°C. Notably, a circle in the plot indicated that the CVN sample with a 279 J absorbed energy did not break apart during impact testing. The absorbed energies at –30°C for the 2.9 kJ/mm and 2.3 kJ/mm samples were less than 150 J. The high values ( $\approx$  246 J) of absorbed energy at –30°C for the 2.6 kJ/mm sample relative to the absorbed energies at –10°C ( $\approx$  200 J) were attributed to the crack path propa-

gating through the FGHAZ and ICHAZ/BM, which is further discussed in the following section. For all samples tested at or below –45°C, the fractures were brittle with low absorbed energies of less than 50 J.

### Analysis of Notch Placement, Crack Path, and Fractography

Sixteen CVN samples impacted at 28°C, –10°C, and –30°C were sectioned (Fig. 5) for notch placement and crack path analysis. Figure 5A shows the center of the notch (the radius of the V notch is 0.25 mm for all samples [Ref. 7]) and OM crack path on the middle thickness plane for the 2.9 kJ/mm sample tested at –10°C (16 J). The length of the notch wall was calculated using the dimensions of the as-received CVN samples (the 45 deg opening angle and 8 mm ligament length

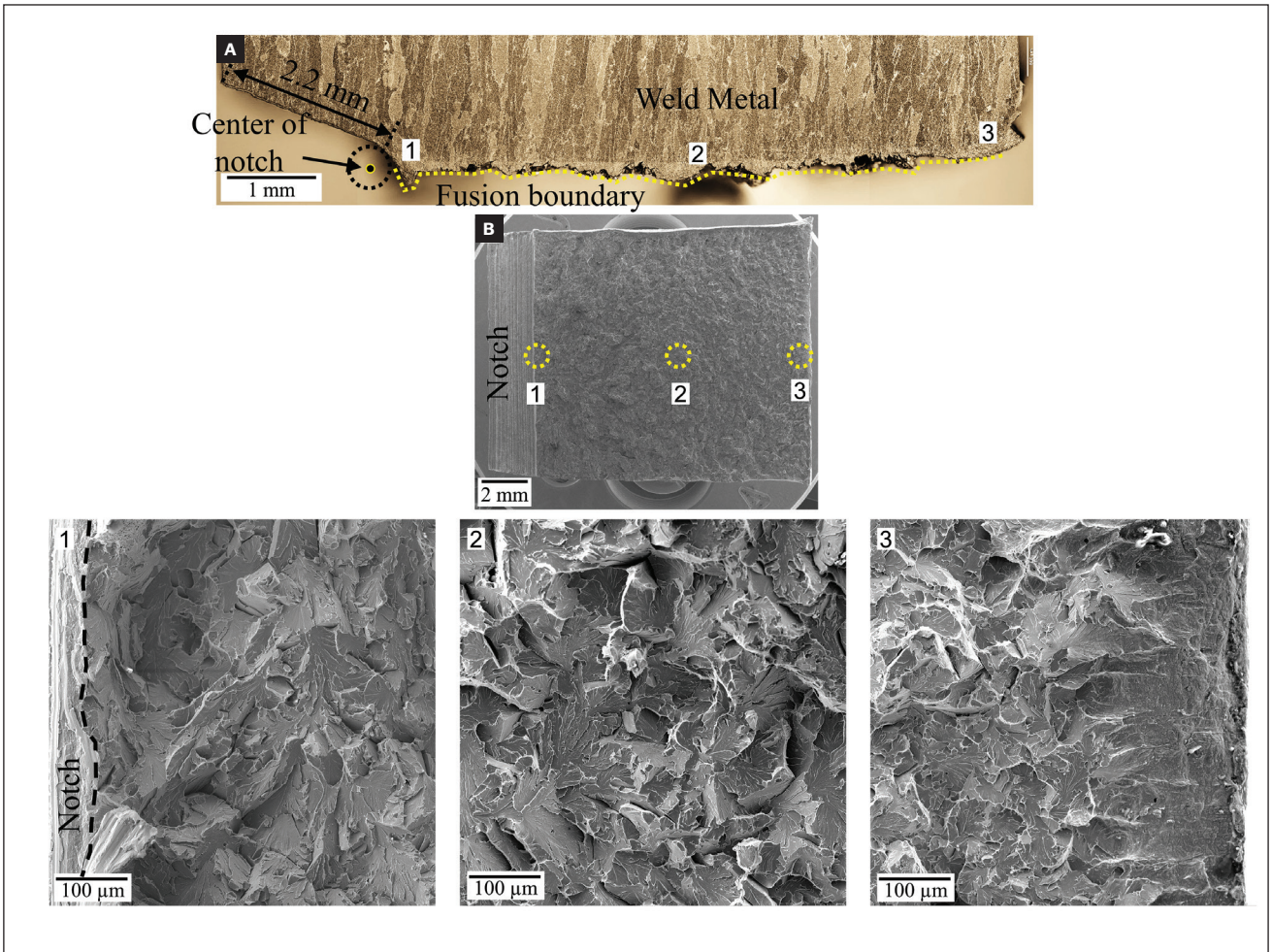


Fig. 7 – Charpy specimen from the 2.3 kJ/mm sample at  $-10^{\circ}\text{C}$  (20 J): A – Optical crack path profile at the middle thickness plane; B – SEM SE images at the fracture surface locations labeled 1, 2, and 3.

shown in Fig. 2). It was determined to be 2.2 mm, as indicated in Fig. 5A. The 2.2 mm notch wall length was used to identify the location of the notch center for notch placement analysis of all sectioned CVN samples. The length of cracking in the fusion boundary was measured using the dotted line along the crack path (Fig. 5A) and was determined to be 8.05 mm ( $L_r$ ) for this sample. Figure 5B is a magnified OM image of the notch tip region in Fig. 5A. The crack was initiated adjacent to the fusion boundary. The distance of the notch tip center from the fusion boundary (Fig. 5B) was measured as 0.1 mm ( $D_{NF}$ ). These length and distance measurements were made for all sectioned samples. Figure 5C is a low-magnification SEM SE image of the fracture surface. Figures 5C-1–3 are higher magnification SEM SE images of the fracture surface corresponding to cracking adjacent to the notch region in the center and final fracture regions (regions 1, 2, and 3), respectively. Figures 5C-1, 2, and 3 show the fracture was completely cleavage.

Figure 6A shows the center of the notch tip and the OM crack path on the middle thickness plane for the 2.6 kJ/mm sample tested at  $-10^{\circ}\text{C}$  (194 J). The center of the notch tip was in the CGHAZ. The crack was initiated in the CGHAZ. Figure 6B is an SEM SE image of the entire fracture surface,

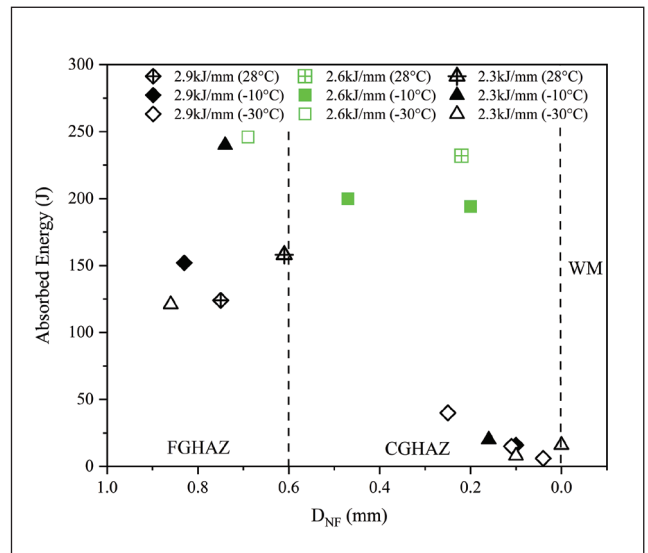


Fig. 8 – Measured absorbed energy and distance from the fusion boundary to the notch placement center ( $D_{NF}$ ) for test temperatures of  $28^{\circ}\text{C}$ ,  $-30^{\circ}\text{C}$ , and  $-10^{\circ}\text{C}$ .

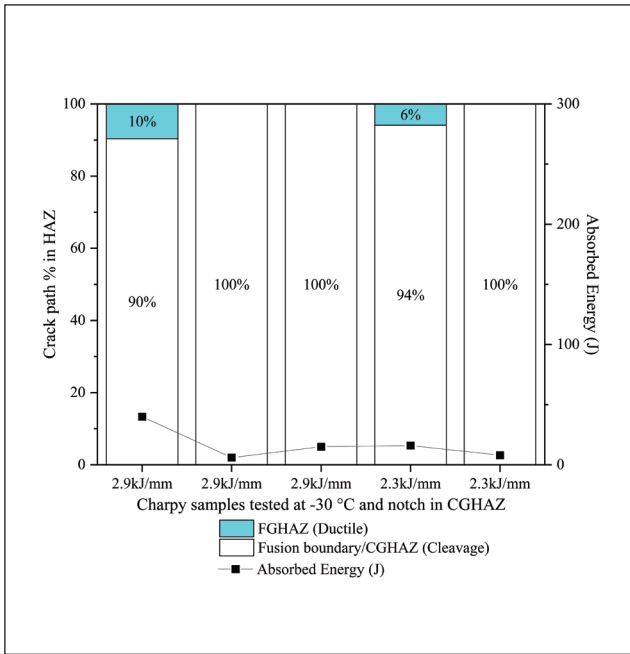


Fig. 9 – Percentage of the crack path in each zone and absorbed energy at  $-30^{\circ}\text{C}$  for the CVN samples with CGHAZ notch placement.

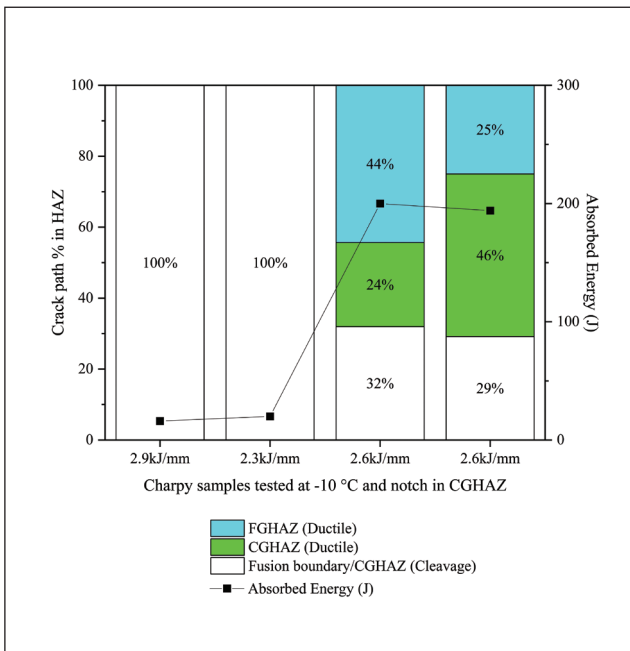


Fig. 10 – Percentage of the crack path in each zone and absorbed energy at  $-10^{\circ}\text{C}$  for the CVN samples with CGHAZ notch placement.

which shows a dull fibrous surface and shear lips indicative of ductile fracture. Figures 6B-1–4 are higher magnification SEM images of the fracture surface corresponding to cracking adjacent to the notch (region 1), the transition from the CGHAZ to the FGHAZ (region 2), and the transi-

tion from the CGHAZ to the fusion boundary (region 3) and final fracture (region 4), respectively. Figures 6B-1 and 6B-2 show that the fracture was ductile. Figure 6B-3 shows the transition from the ductile fracture to cleavage (CGHAZ to fusion boundary). The fracture at the fusion boundary (Fig. 6B-3) was complete cleavage. Fig. 6B-4 shows the ductile dimples in the final fracture.

Based on the similar HAZ width at the quarter thickness ( $\sim 4$  mm below the weld surface) of all welds in the transverse direction (HAZ images for the 2.9 kJ/mm and 2.6 kJ/mm samples are shown in Fig. 1 and Fig. 2, respectively), the CGHAZ-FGHAZ interface was identified at a location with a distance of 0.6 mm from the fusion boundary. The 0.6 mm distance (e.g., in Fig. 6A) was used to identify the CG/FGHAZ interface for all sectioned CVN samples.

Figure 7A shows the center of the notch tip and the OM crack path on the middle thickness plane for the 2.3 kJ/mm sample tested at  $-10^{\circ}\text{C}$  (20 J). The lower magnification SEM image (Fig. 7B) shows the fracture surface. The higher magnification SEM SE images (Figs. 7B-1, 7B-2, and 7B-3) show the fracture surface corresponding to cracking adjacent to the notch (region 1), the center (region 2), and the final fracture (region 3), respectively. All images show predominant cleavage fracture on the entire fracture surface. Qualitatively, the 2.6 kJ/mm sample exhibited more ductile fracture behavior than the 2.9 kJ/mm and 2.3 kJ/mm samples tested at  $-10^{\circ}\text{C}$ .

Table 1 summarizes the measured distances of the notch center from the fusion boundary ( $D_{NF}$ ) and the crack path lengths in each zone of the HAZ for all broken CVN samples at  $-30^{\circ}\text{C}$ , six CVN samples at  $-10^{\circ}\text{C}$ , and three CVN samples at  $28^{\circ}\text{C}$ . The samples were chosen to allow detailed characterization of failures with a full range of Charpy energies to develop a better understanding of notch placement and crack path results. For simplicity, the measured crack path lengths in each zone of the HAZ, with its observed fracture mechanisms, are defined in three ways: crack lengths in the fusion boundary/CGHAZ region with cleavage fracture ( $L_{F/CG-C}$ ), crack lengths in the CGHAZ with ductile fracture ( $L_{CG-D}$ ), and crack lengths in the FGHAZ with ductile fracture ( $L_{FG}$ ). Of note is that the  $L_{FG}$  of the 2.6 kJ/mm sample at  $-30^{\circ}\text{C}$  (246 J) is the sum of the measured crack lengths in the FGHAZ and ICHAZ/BM region because the fracture was consistently ductile for the entire fracture surface. The absorbed energy of each sectioned CVN sample was plotted against  $D_{NF}$  and the percentage of the measured crack path in the HAZ, which is presented next.

Figure 8 shows the absorbed energy versus  $D_{NF}$  measurements for all sectioned CVN samples at  $-10^{\circ}\text{C}$ ,  $-30^{\circ}\text{C}$ , and  $28^{\circ}\text{C}$ . The absorbed energies for the 2.9 kJ/mm and 2.3 kJ/mm samples at  $-10^{\circ}\text{C}$  and  $-30^{\circ}\text{C}$  increased significantly as  $D_{NF}$  increased (notch in the FGHAZ). Alternatively, the 2.6 kJ/mm samples showed consistently high absorbed energy values ( $> 190$  J) at both test temperatures with varied  $D_{NF}$  (notch in the CGHAZ or FGHAZ). The absorbed energy results for the 2.9 kJ/mm and 2.3 kJ/mm samples were widely scattered at  $-10^{\circ}\text{C}$  and  $-30^{\circ}\text{C}$ , possibly related to the CG/FGHAZ microstructure in the notch tip region. Conversely, the high absorbed energy results at  $28^{\circ}\text{C}$ ,  $-10^{\circ}\text{C}$ , and  $-30^{\circ}\text{C}$  for the 2.6 kJ/mm samples were independent of  $D_{NF}$ . The correlation

of notch placement in the CGHAZ with Charpy toughness is discussed in the “Discussion” section.

Figures 9 and 10 show the percentage of the crack path in each zone of the HAZ at  $-30^{\circ}\text{C}$  and  $-10^{\circ}\text{C}$ , respectively, for all CVN samples with the notch placement in the CGHAZ. In Fig. 9, the fracture paths of the 2.9 kJ/mm and 2.3 kJ/mm CVN samples consisted of  $\geq 90\%$  cleavage fracture in the fusion boundary/CGHAZ region, which resulted in relatively low absorbed energy values ( $< 50$  J). The low absorbed energy indicated that cleavage was easily initiated in the CGHAZ of the 2.9 kJ/mm and 2.3 kJ/mm samples during Charpy testing, which is linked to the large size of MA constituents. According to Chen et al. (Ref. 8), larger MA constituents in the CGHAZ result in lower local loads needed to initiate new cleavage cracks due to increased local stress concentration and triaxial stress state at the MA-ferrite interface. Additionally, cleavage propagation occurs by connecting multiple micro-cracks that start at the MA-ferrite interface or in the cracked MA (Ref. 8). This explains why the larger MA distribution (in terms of MA size and Area fraction) accounted for the  $\geq 90\%$  cleavage fracture in the fusion boundary/CGHAZ region of the 2.9 kJ/mm and 2.3 kJ/mm CVN samples.

The crack path in the HAZ of the 2.9 kJ/mm and 2.3 kJ/mm CVN samples at  $-10^{\circ}\text{C}$  was 100% cleavage fracture, as shown in Fig. 10. The absorbed energy was  $< 25$  J, which was similar to the  $-30^{\circ}\text{C}$  results in Fig. 9. On the other hand, the fracture path of the 2.6 kJ/mm CVN samples exhibited  $\sim 70\%$  ductile fracture in the CGHAZ and FGHAZ, which led to high absorbed energies ( $\sim 200$  J). The finer MA distribution in the CGHAZ of 2.6 kJ/mm samples inhibited cleavage initiation at the MA-ferrite interface during Charpy testing due to lower local stress concentration. All MA morphology results in both the CGHAZ and FGHAZ were used to study the effect of complex MA morphology on Charpy toughness using a proposed MA severity parameter. Detailed formulation and results are provided in the following section.

## Discussion

### Notch Placement in the CGHAZ and Absorbed Energy

In Figs. 8–10, all 2.9 kJ/mm and 2.3 kJ/mm CVN samples tested showed  $> 90\%$  cleavage fracture at both  $-10^{\circ}\text{C}$  and  $-30^{\circ}\text{C}$  and cracks propagated along the area adjacent to the fusion boundary when the notch placement was in the CGHAZ or adjacent to the fusion boundary. It is worth noting that tested 2.6 kJ/mm CVN specimens notched in the CGHAZ (close to the fusion boundary) showed adjacent crack initiation. Then, the crack deflected to the FGHAZ (Fig. 6A). Ductile dimples were observed in the CGHAZ and FGHAZ at the crack initiation stage until the transition to the CGHAZ/fusion boundary, which resulted in high absorbed energies (Figs. 6B-1 and 6B-2). Since all welds had similar bainitic microstructures in the CGHAZ (shown in Fig. 3 in the “Results” section of Part 1 (Ref. 1), the ductile fracture behavior in the CGHAZ of the 2.6 kJ/mm samples versus the cleavage fracture behavior in the CGHAZ (close to the

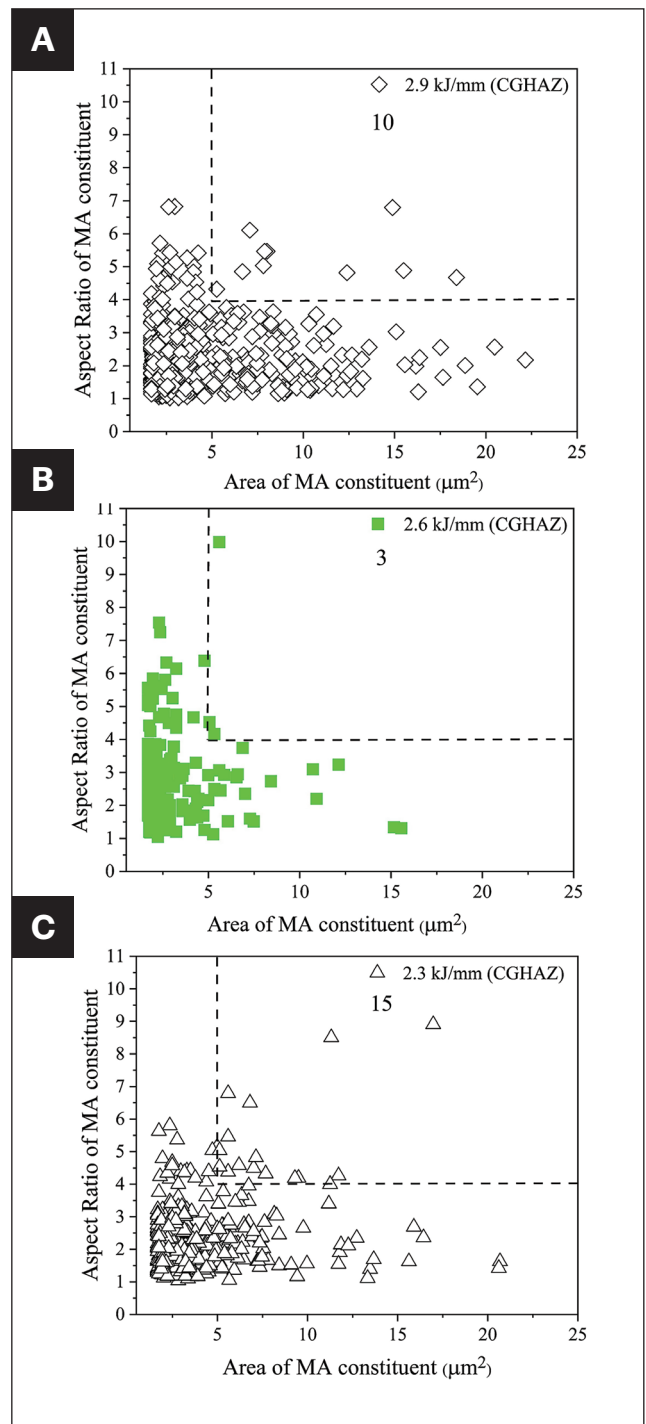


Fig. 11 — MA aspect ratio vs. Area of MA constituents in the CGHAZ: A — 2.9 kJ/mm; B — 2.6 kJ/mm; C — 2.3 kJ/mm. The number of coarse-stringer MA constituents is indicated in the top-right quadrant.

fusion boundary) of the 2.9 kJ/mm and 2.3 kJ/mm samples indicated that MA morphology has a significant effect on absorbed energy, which will be discussed next.

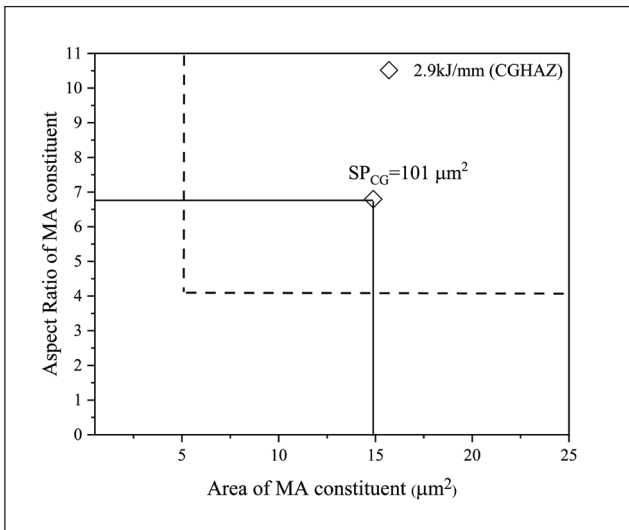


Fig. 12 – Example of the severity parameter ( $SP_{CG}$ ) for a single coarse-stringer MA constituent in the CGHAZ of the 2.9 kJ/mm sample. The  $SP_{CG}$  value of  $101 \mu\text{m}^2$  is the area of the solid rectangle.

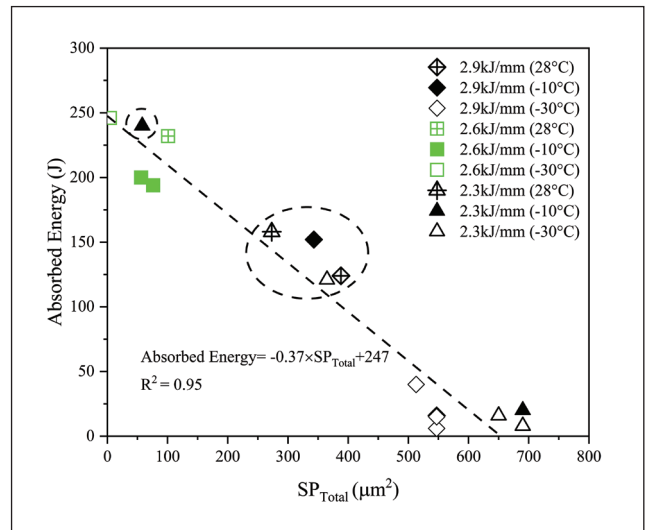


Fig. 13 – Absorbed energy at 28°C, -10°C, and -30°C vs. total severity parameter ( $SP_{Total}$ ) for the CVN samples.

**Table 2 – Severity Parameter for the Overall Coarse-Stringer MA Constituents (Area > 5  $\mu\text{m}^2$  and AR > 4) in the CGHAZ ( $SP_{CG}$ ) and FGHAZ ( $SP_{FG}$ ) of All Welds**

	$SP_{CG}$ ( $\mu\text{m}^2$ )	$SP_{FG}$ ( $\mu\text{m}^2$ )
2.9 kJ/mm	547	192
2.6 kJ/mm	101	0
2.3 kJ/mm	690	0

## Correlating MA Morphology with Charpy Toughness

The complex morphology of MA constituents can be characterized by their AR and area. Yang et al. (Ref. 9) observed that debonded and cracked coarse MA constituents along the crack propagation path had a similar morphology. These MA constituents were mostly responsible for deteriorated fracture toughness. These constituents were classified as coarse-stringer-like (Area > 5  $\mu\text{m}^2$  and AR > 4) MA constituents. They concluded that coarse-stringer MA constituents tend to initiate microcracks due to the increased local stress concentration and low critical stress required for microcrack formation. Chen et al. (Ref. 8) and Xie et al. (Ref. 10) also confirmed the same morphology of coarse-stringer MA constituents. They observed detached MA from the ferrite matrix and fractured MA by secondary micro-cracks, which facilitated/promoted crack propagation. This study defines coarse-stringer MA constituents as those with an MA Area > 5  $\mu\text{m}^2$  and an MA AR > 4 and correlated to fracture behavior through a newly developed severity parameter.

The Area and AR distributions for MA in the CGHAZ and FGHAZ for all welds were presented in detail in the “Results” section of Part I of this article (Ref. 1). Figure 11 plots the MA AR versus MA Area in the CGHAZ for all welds. Figure 11A (2.9 kJ/mm) and 11C (2.3 kJ/mm) show a large number (10 and 15, respectively) of coarse-stringer MA features (Area > 5  $\mu\text{m}^2$  and AR > 4) in the upper right quadrant of each graph. Conversely, the number of coarse-stringer MA features for 2.6 kJ/mm was relatively small (3). The relatively large number of coarse-stringer MA features in the CGHAZ for both the 2.9 kJ/mm and 2.3 kJ/mm samples could increase the likelihood of cleavage crack initiation at the grain/lath boundaries due to increased local stress concentration (Refs. 10–12). The low number of coarse-stringer MA features in the CGHAZ of the 2.6 kJ/mm samples should make this weld less susceptible to cleavage crack initiation.

To assess the overall effect of coarse-stringer MA constituents (in the upper right quadrant of each graph in Fig. 11) on Charpy absorbed energies, an MA severity parameter (SP) is proposed that quantifies the cumulative severity of all coarse-stringer MA constituents. The general form of the SP is shown in Equation 1 for the CGHAZ and Equation 2 for the FGHAZ:

$$SP_{CG,i} = \sum_{j=1}^n (AR_{CG,i} * Area_{CG,i}) \quad (1)$$

$$SP_{FG,i} = \sum_{j=1}^n (AR_{FG,i} * Area_{FG,i}) \quad (2)$$

where  $i$  is a specific weld (e.g., 2.9 kJ/mm),  $j$  is a specific coarse-stringer MA constituent ( $Area > 5 \mu\text{m}^2$  and  $AR > 4$ ), and  $n$  is the total number of coarse-stringer MA features.  $AR_j$  is the AR and  $Area_j$  is the Area for each individual coarse-stringer MA constituent ( $j$ ) in the CGHAZ or FGHAZ. The SP calculated for an individual MA increases with an increase in size (MA Area) and AR. An example of the SP for a single coarse-stringer MA ( $Area = 14.9 \mu\text{m}^2$  and  $AR = 6.8$ ) in the CGHAZ of 2.9 kJ/mm is shown in Fig. 12 and has an  $SP_{CG} = 101 \mu\text{m}^2$ , which is the area of the rectangle shown.

$SP_{CG}$  and  $SP_{FG}$  values for all welds were determined and are shown in Table 2. The  $SP_{CG}$  was highest at 2.3 kJ/mm ( $690 \mu\text{m}^2$ ) and lowest at 2.6 kJ/mm ( $101 \mu\text{m}^2$ ). The low  $SP_{CG}$  for the 2.6 kJ/mm sample was attributed to both the low total number of coarse-stringer MA constituents and their small Areas and ARs. For all Charpy tests with a  $D_{NF}$  less than 0.6 mm (in the CGHAZ and adjacent to the fusion boundary), the  $SP_{CG}$  of the coarse-stringer MA in the CGHAZ strongly influenced the Charpy absorbed energy and crack propagation path. For both the 2.9 kJ/mm and 2.3 kJ/mm welds, the high  $SP_{CG}$  values corresponded to crack initiation in the CGHAZ adjacent to the fusion boundary and subsequent propagation. Conversely, a low  $SP_{CG}$  value (2.6 kJ/mm) resulted in the crack deflecting away from the fusion line (Fig. 6A). Low  $SP_{FG}$  values (all welds) corresponded to high absorbed energies ( $> 120 \text{ J}$ ) for CVN samples with  $D_{NF}$  greater than 0.6 mm (in the FGHAZ).

The  $SP_{CG}$  and  $SP_{FG}$  values shown in Table 2 were combined with the crack length ratio in either the CGHAZ or the FGHAZ to calculate an overall severity parameter ( $SP_{Total}$ ) for each CVN test, according to Equation 3:

$$SP_{Total,k} = \frac{L_{F/CG,k}}{L_{Total,k}} * SP_{CG,i} + \frac{L_{FG,k}}{L_{Total,k}} * SP_{FG,i} \quad (3)$$

where  $L_{F/CG}$  and  $L_{FG}$  are measured crack lengths in the fusion boundary/CGHAZ and FGHAZ and  $L_{Total}$  is the total crack length (shown in Table 1);  $k$  represents a specific CVN sample. Figure 13 plots the CVN energy as a function of  $SP_{Total}$  and the data shows a linear trend where absorbed energy during Charpy testing decreased as the total severity parameter increased. Both the 2.9 kJ/mm and 2.3 kJ/mm CVN samples exhibited large  $SP_{Total}$  values ( $> 250 \mu\text{m}^2$ ) in combination with large crack ratios in the CGHAZ and small crack ratios in the FGHAZ. As such, the absorbed energy values were low ( $< 50 \text{ J}$ ). The 2.6 kJ/mm CVN samples had small  $SP_{Total}$  values ( $< 40 \mu\text{m}^2$ ), which corresponded to high absorbed energies ( $> 190 \text{ J}$ ) due to the relatively small  $SP_{CG}$  and  $SP_{FG}$  values. Of particular note is that the 2.9 kJ/mm and 2.3 kJ/mm CVN

samples, with high absorbed energy values ( $> 100 \text{ J}$  - circled in Fig. 13), had high crack ratios in the FGHAZ (Table 1). It is acknowledged that crystallographic characteristics (such as grain misorientation, sub-grain size, etc.) can also influence toughness. That is the subject of future work.

## Conclusions

The effect of martensite-austenite constituent morphology and prior austenite grain size on the Charpy toughness of cold-wire tandem submerged-arc welded X70 steel was studied. Three levels of effective heat inputs (cold wire feed rates) were utilized for welding, corresponding to 2.9 kJ/mm (0 mm/s), 2.6 kJ/mm (16.9 mm/s), and 2.3 kJ/mm (33.9 mm/s). A new parameter — i.e., the total severity parameter ( $SP_{Total}$ ) for coarse-stringer MA constituents ( $Area > 5 \mu\text{m}^2$  and  $AR > 4$ ) — was introduced to correlate the complex MA morphology and crack length ratio with Charpy absorbed energy in the HAZ. The main conclusions are summarized as follows:

1. An intermediate effective heat input (2.6 kJ/mm) resulted in an intermediate PAG size and a small number of coarse-stringer MA constituents (a detrimental MA morphology) in the CGHAZ. As such, cleavage fracture in the CGHAZ was inhibited, and high Charpy energies ( $> 120 \text{ J}$ ) in the HAZ at low temperatures ( $-10^\circ\text{C}$  and  $-30^\circ\text{C}$ ) were obtained.

2. Both high effective heat input (2.9 kJ/mm) and low effective heat input (2.3 kJ/mm) led to a large number of coarse-stringer MA constituents in the CGHAZ, which facilitated cleavage initiation and propagation in the CGHAZ. The Charpy energies in the HAZ were reduced at low temperatures ( $< 45 \text{ J}$ ).

3. The calculation of  $SP_{Total}$  accounted for the overall effect of coarse-stringer MA constituents and crack path in the HAZ, which can provide the overall impact of coarse-stringer MA constituents in the HAZ.

4. A low  $SP_{Total}$  range ( $2-40 \mu\text{m}^2$ ) was representative of a fine MA distribution with low numbers of coarse-stringer MA constituents and a large crack length ratio in the FGHAZ. A low  $SP_{Total}$  also correlated with high Charpy impact energies ( $> 120 \text{ J}$ ) in the HAZ.

5. A high  $SP_{Total}$  range ( $250-350 \mu\text{m}^2$ ) corresponded to a concentrated and coarse-stringer MA distribution, including a large number of coarse-stringer MA constituents and a large crack length ratio in the fusion boundary/CGHAZ, which reduces Charpy impact energies ( $< 45 \text{ J}$ ) in the HAZ.

6. A low  $SP_{Total}$  range corresponded to steels welded with an intermediate effective heat input of 2.6 kJ/mm. In comparison, a high  $SP_{Total}$  range corresponded to steels welded with a high effective heat input of 2.9 kJ/mm and a low effective heat input of 2.3 kJ/mm.

## Acknowledgments

The authors would like to acknowledge the financial support of the Natural Sciences and Engineering Research Council (NSERC) of Canada, Evraz Inc. NA, and TC Energy Corp. The assistance of Mohsen Mohammadijoo with welding trials is appreciated. The R&D Division of Evraz Inc. NA is recognized for providing welding equipment and technical assistance in conducting welding trials and CVN testing.

## References

1. Ren, T., Wiskel, J. B., Lehnhoff, G., Ivey, D. G., Li, L., Collins, L., Gaudet, M., Willett, E., and Henein, H. 2025. Effect of microstructure on toughness for CWTSAW heavy gauge X70 Part 1 – Microstructure characterization and quantification. *Welding Journal* 104(3): 94-s to 105-s. DOI: 10.29391/2025.104.008
2. Li, C., Wang, Y., and Chen, Y. 2011. Influence of peak temperature during in-service welding of API X70 pipeline steels on microstructure and fracture energy of the reheated coarse grain heat-affected zones. *Journal of Materials Science* 46(19): 6424–6431. DOI: 10.1007/s10853-011-5592-7
3. Li, C., Wang, Y., Han, T., Han, B., and Li, L. 2011. Microstructure and toughness of coarse grain heat-affected zone of domestic X70 pipeline steel during in-service welding. *Journal of Materials Science* 46(3): 727–733. DOI: 10.1007/s10853-010-4803-y
4. Lambert-Perlade, A., Drillet, J., Gourgues, A. F., Sturel, T., and Pineau, A. 2000. Microstructure of martensite-austenite constituents in heat affected zones of high strength low alloy steel welds in relation to toughness properties. *Science and Technology of Welding and Joining* 5(3): 168–173. DOI: 10.1179/136217100101538164
5. Ren, T. 2021. Effect of cold wire TSAW on weld geometry and CGHAZ microstructure of heavy gauge X70. Master's thesis, University of Alberta. DOI: 10.7939/r3-qsjk-ej65
6. ASTM International. ASTM E384-17. 2017, *Standard Test Method for Microindentation Hardness of Materials*. Retrieved from [astm.org/e0384-17.html](http://astm.org/e0384-17.html).
7. ASTM International. ASTM E23-18. 2013, *Standard Test Methods for Notched Bar Impact Testing of Metallic Materials*. Retrieved from [webstore.ansi.org/standards/astm/astme2318](http://webstore.ansi.org/standards/astm/astme2318).
8. Chen, J. H., Kikuta, Y., Araki, T., Yoneda, M., and Matsuda, Y. 1984. Micro-fracture behaviour induced by M-A constituent (Island Martensite) in simulated welding heat affected zone of HT80 high strength low alloyed steel. *Acta Metallurgica* 32(10): 1779–1788. DOI: 10.1016/0001-6160(84)90234-7
9. Yang, X., Di, X., Liu, X., Wang, D., and Li, C. 2019. Effects of heat input on microstructure and fracture toughness of simulated coarse-grained heat affected zone for HSLA steels. *Materials Characterization* 155(9): 109818. DOI: 10.1016/j.matchar.2019.109818
10. Xie, C., Liu, Z., He, X., Wang, X., and Qiao, S. 2020. Effect of martensite-austenite constituents on impact toughness of pre-tempered MnNiMo bainitic steel. *Materials Characterization* 161. DOI: 10.1016/j.matchar.2020.110139
11. Li, X., Fan, Y., Ma, X., Subramanian, S. V., and Shang, C. 2015. Influence of martensite-austenite constituents formed at different intercritical temperatures on toughness. *Materials and Design* 67: 457–463. DOI: 10.1016/j.matdes.2014.10.028
12. Huda, N., Wang, Y., Li, L., and Gerlich, A. P. 2019. Effect of martensite-austenite (MA) distribution on mechanical properties of inter-critical reheated coarse grain heat affected zone in X80 linepipe steel. *Materials Science and Engineering A* 765(2): 138301. DOI: 10.1016/j.msea.2019.138301

**TALIN REN** ([tailin@ualberta.ca](mailto:tailin@ualberta.ca)), **J. BARRY WISKEL**, **DOUGLAS G. IVEY**, **LEIJUN LI**, and **HANI HENEIN** are with the Department of Chemical and Materials Engineering, University of Alberta, Edmonton, Alberta, Canada. **LAURIE COLLINS** is with (formerly) the R&D Division, EVRAZ North America, Regina, Saskatchewan, Canada. **GREG LEHNHOFF** and **MICHAEL GAUDET** are with the R&D Division, EVRAZ North America, Regina, Saskatchewan, Canada. **ERIC WILLETT** is with TC Energy Corp., Calgary, Alberta, Canada.